

Mechanical Properties of Highly Deformable Elastomeric Gyroids for Multifunctional Capacitors

Emilie R. Baker Khoi Ly Nikola Bosnjak Maura R. O'Neill Rachel Miller Sandra Li Robert F. Shepherd* Meredith N. Silberstein*

E. R. Baker, Dr. K. Ly, Dr. N. Bosnjak, M. R. O'Neill, S. Li, Prof. R. F. Shepherd, Prof. M. N. Silberstein

Department of Mechanical and Aerospace Engineering, Cornell University, Ithaca, NY 14850, USA

Email Address: rfs247@cornell.edu, ms2682@cornell.edu

R. Miller

Department of Materials Science and Engineering, Cornell University, Ithaca, NY 14850, USA

Keywords: *Triply Periodic Minimal Surfaces, Elastomeric Metamaterials, Gyroid Capacitor, Additive Manufacturing, Embodied Energy*

Triply periodic minimal surface lattices have mechanical properties that derive from the unit cell geometry and the base material. Through computation software like nTopology and Abaqus, we can use these geometries to tune nonlinear stress-strain curves not readily achievable with solid materials alone and to change the compliance by two orders of magnitude compared to the constituent material. In this study, four elastomeric TPMS gyroids undergo large deformation compression and tension testing to investigate the impact of the structure's geometry on the mechanical properties. Amongst all the samples, the modulus at strain $\varepsilon = 0.05$ varied by over one order of magnitude (7.7 to 293.4 kPa from FEA under compression). These lattices are promising candidates for designing multifunctional systems that can perform multiple tasks simultaneously by leveraging the geometry's large surface area to volume ratio. For example, we can combine the architectural functionality of the lattice to bear loads and store mechanical energy along with the larger surface area for energy storage. We demonstrate a compliant double gyroid capacitor that can simultaneously achieve three functions: load bearing, energy storage, and sensing.

1 Introduction

A metamaterial derives its mechanical properties not only from its material but also from its geometry [1, 2, 3]. Applications include tissue engineering [4, 5, 6], actuators [7, 8, 9, 10, 11, 12, 13], heat exchangers [14, 15], and energy storage devices [16, 17]. Metamaterials can modify the mechanical [18, 19, 20, 21, 22, 23, 24], electrical [16, 17, 25], acoustic [26, 27, 28, 29, 30, 31], optical [32, 33, 34], fluidic [35, 36], and thermal [14, 15, 37] behavior of devices and structures. Triply periodic minimal surface (TPMS) lattices are a well defined subcategory of metamaterials. TPMS refers to geometry that repeats in three dimensions (triply periodic), and the surface has a constant mean curvature of zero at every point (minimal surface) [38].

This is the author manuscript accepted for publication and has undergone full peer review but has not been through the copyediting, typesetting, pagination and proofreading process, which may lead to differences between this version and the [Version of Record](#). Please cite this article as [doi: 10.1002/adem.202300629](https://doi.org/10.1002/adem.202300629).

This article is protected by copyright. All rights reserved

The goal of this work is to show how TPMS lattices stand out from other metamaterials as promising candidates for multifunctional system designs by using both their mechanical robustness (for mechanical tuning of a structure) and importantly their large surface area to volume ratio. TPMS lattices can make i. mechanically robust composites because of how they separate space into continuous and intertwined regions, and ii. valuable multiphysics systems because of their large surface area to volume ratio. Large surface area creates a larger interaction site that can be leveraged in different energy domains for increased chemical activity, faster diffusion rates, faster heat transfer, larger electric fields, and larger magnetic fields. Multifunctional systems and embodied energy systems, systems that combine structural functionality with energy storage[39], are attractive solutions for addressing the limited onboard energy storage, adaptability, functionality, and efficiency of devices and robots.

In this paper, we look at the TPMS lattice known as the gyroid, which was discovered by Alan Schoen in 1970[40]. The equations shown in **Figure 1A** approximate the gyroid's geometry. First, we study the mechanical properties of the gyroid. We wrote Python scripts to automate commercial software for easy to produce 3D printer files and finite element (FE) mesh files. After generating the FE mesh files, a second software script runs a finite element analysis (FEA) for both compression and tension loading conditions with strains of $\varepsilon = \pm 0.5$. We define strain as $\varepsilon = \Delta H * H_0^{-1}$ where H is height. We analyze four different gyroid unit cells. The lattices are composites of elastomer and air.

TPMS structures often have complex geometries that are more easily fabricated with additive manufacturing. Advances in digital light processing (DLP), a type of 3D printing, enable a range of materials to be 3D printed, including resilient elastomers. By producing elastomeric lattice structures, we are able to tune mechanical properties by leveraging: i. the elastomeric material's ability to return to the undeformed configuration after removing loads and ii. the TPMS structure's ability to tune the stress-strain response. As DLP printers are limited in their ability to produce resilient multi-material parts, the utility of the lattices affects similar outcomes as multi-materials while using only one chemistry in addition to producing nonlinear stress-strain curves not readily achievable with either solid materials or multi-material parts. Experimental tests using 3D printed silicone urethane elastomeric parts validate the FEA results. **Figure 1A** provides the project overview.

The most compliant and most stiff gyroids have a modulus at $\varepsilon = 0.05$ that varies by over one order of magnitude (7.7-293.4 kPa under compression and 10.7-282.1 kPa under tension) for volume fractions, $\phi = V_{gyroid} * V_{cube}^{-1}$, between 0.1-0.46 (where V_{gyroid} is volume occupied by the gyroid and V_{cube} is the volume of the cube enclosing the gyroid). Using the mechanical analysis, we design, print, and test a compliant gyroid capacitor. The capacitor is a multifunctional embodied energy system because it combines structural functionality (large compliance), electrical energy storage (capacitor), and self sensing (ability to measure changes in capacitance with deformation).

2 Materials and Methods

2.1 Designing Gyroids

TPMS geometries, like the gyroid, can be approximated using mathematical equations [41, 42]. Equation (1) defines the surface of the single gyroid in 3D space

$$U_{SG}(x, y, z) \equiv S_x C_y + S_y C_z + S_z C_x = t \quad (1)$$

where t is a function of the volume fraction. S and C are short hand notations for sine and cosine,

$$S_i = \sin(k_i i L_i^{-1}) \quad (\text{with } i = x, y, z) \quad (2)$$

$$C_i = \cos(k_i i L_i^{-1}) \quad (\text{with } i = x, y, z) \quad (3)$$

where x , y , and z are coordinate directions, and L_i is the length of the unit cell in each direction. k_i is the lattice function periodicity,

$$k_i = 2\pi n_i \quad (\text{with } i = x, y, z) \quad (4)$$

where n_i is the number of unit cells in each direction. Equation (1) produces the geometries in **Figure 1Bi-ii** and divides space into two regions. We indicate the region formed by **Figure 1Bi** as single gyroid positive (SGp) and the void region as single gyroid negative (SGn) in **Figure 1Bii**. SGp and SGn have opposite chirality, and if added together, they form a solid cube given the same t value. The double gyroid (DG) divides space into three regions. The matrix (DGm) separates two void regions that form two separate networks (DGn) as shown in **Figure 1Biii-iv**. The following equation (5) defines the surface of the double gyroid

$$U_{DG}(x, y, z) \equiv (S_x C_y + S_y C_z + S_z C_x)^2 = t^2 \quad (5)$$

where t is once again directly related to the volume fraction. Equation (5) produces the geometries in **Figure 1Biii-iv**. **Figure 1C** shows the correlation between t and volume fraction.

nTopology, a commercial software, can define geometry by mathematical expressions. Scripting nTopology automates the production of many geometry variations quickly and easily by controlling inputs like the equation. We select four gyroid variations for this study including SGp (with t values equal to -1.2 and 0.0) and DGm (with t values equal to 0.2 and 0.7). Table 1 lists the naming convention and volume fraction of elastomer. We study SGp and DGm because they are the base components of all the gyroid variations. For example, SGn has opposite chirality from SGp, and DGn is the combination of SGp and SGn (given the correspond t parameters like SGp-1.2 and SGn1.2). Additionally, we select SGp and DGm lattices to provide cleaner and more reliable results for both printing and simulation of low and high volume fraction lattices. For printing the DGn, more fabrication challenges arise for low volume fractions (smaller struts) and high volume fractions (preventing connections between networks). For simulations two networks lead to more contact interactions, which can greatly increase the computational cost and make convergence more difficult. In this study, the length of the unit cells, L_i , is 10 mm in each direction (x, y, z). We chose the values of t and L_i based upon printability and interest in looking at highly compliant, porous structures. After defining the geometric parameters, the software exports print files (.stl) and finite element mesh files (.inp for Abaqus).

2.2 FEA Simulations

By scripting Abaqus, a commercial FEA software, the user can automate finite element analysis with Python programming language. The material model used to approximate the behavior of the elastomer is a Yeoh third order hyperelastic material model. **Figure 1D** shows a good fit between the material model and the experimental tension data supplied by Carbon 3D for SIL-30, a silicone urethane elastomer. The mesh file from nTopology consists of linear tetrahedral hybrid elements (C3D4H). To reduce computation time, the analysis uses a single unit cell of each gyroid. We apply periodic boundary conditions to account for the larger system of the composite. To apply periodic boundary conditions, dummy nodes constrain the nodes on the corners, edges, and faces of the unit cells [43, 44]. The dummy nodes are either free, fixed, or stepped to 5 mm of displacement ($\varepsilon = 0.5$ engineering strain) to mimic the compression and tension boundary conditions of the experimental tests (SI Appendix, Figure S1). Lastly, contact interactions prohibit self penetration as the geometry deforms.

2.3 Experimental Testing

This article is protected by copyright. All rights reserved

The experimental compression samples consist of 5 x 5 x 5 unit cells, which results in dimensions of 50 x 50 x 50 mm. The experimental tension samples consist of 3 x 3 x 10 unit cells, which results in dimensions of 30 x 30 x 100 mm. For each test mode, compression and tension, there are three specimens for each geometry listed in Table 1. We print, cure, and test every sample in the z-direction as defined by equations (1) and (5). We use a Carbon 3D M1 printer with SIL 30 (a silicone urethane resin) for printing, clean the parts with isopropyl alcohol for 5 minutes, leave the parts air dry for at least 12 hours, and then place the parts in a salt bath during the heat treatment (8 hours at 120°). The salt bath is for preserving the dimensions and shape of the samples during the heat treatment. For the experimental setup, we use a Zwick/Roell Z010 testing system, with a 500 N load cell, that collects force and strain data. The specimens underwent three cycles at a strain rate of 1 % s⁻¹ until $\varepsilon = 0.5$ was reached. To understand some of the discrepancies between the FEA and the experimental results, micro-computed tomography (μCT) scans provide visual understanding to identify the differences between the 3D printed and computer generated structures.

2.4 Capacitor

Capacitance, for example, can be increased by having larger surface area electrodes. Using equations not specific to any geometry, the equation for capacitance is

$$C = Q / \Delta V \quad (6)$$

where Q is the charge, and ΔV is the potential difference. Potential difference is given by:

$$\Delta V = V_- - V_+ = \int_+^- E dl \quad (7)$$

where E is electric field, and dl is the differential displacement vector between the positive and negative electrodes. We can calculate the electric field everywhere using Gauss's Law

$$EdA = Q\varepsilon_r^{-1}\varepsilon_0^{-1} \quad (8)$$

where dA is an infinitesimal amount of area on the surface, Q is charge, ε_r is relative permittivity, and ε_0 is vacuum permittivity. From these equations, the larger the surface area of the electrodes and/or smaller the distance between the electrodes the larger the capacitance. To demonstrate both the mechanical robustness and large surface area, we fabricate a gyroid capacitor.

A compliant capacitor demonstrates the multifunctionality of the gyroid lattice and consists of three sections. One section is the capacitor: a double gyroid network with a t value equal to 1.2 (DGn1.2). The DGn1.2 consists of 1 x 3 x 3 unit cells resulting in dimensions of 10 x 30 x 30 mm. The other two sections are solid rectangular prisms for applying loads in the FEA or for gripping the physical device in tension during the experiment. For the FEA of the device, we create the mesh file for the DGn1.2 with 1 x 3 x 3 unit cells using nTopology. Next, Abaqus uses the finite element mesh for pulling the capacitor in tension. We fix one solid rectangular prism and apply a displacement in 1 mm increments to the other prism. Then, we use COMSOL multiphysics, a finite element software. COMSOL calculates the capacitance with an electrostatics analysis using the deformed mesh files (relative permittivity of 3.2 for the dielectric and 1 for the electrodes). To validate the FEA results, we perform an experiment. We print the DGn1.2 capacitor with the same material and process as the rest of the parts in this paper, and afterward, we apply carbon paint (DAG-T-502, TED PELLA INC.) onto the networks using a brush. The carbon paint makes the network conductive and thus forms the compliant electrodes of the capacitor. For testing purposes, we use super glue to bond the device to a container that we fill with a vegetable based liquid dielectric (Envirotemp FR3, $\varepsilon_r = 3.2$). A handheld LCR meter (KEYSIGHT U1733C) measures the capacitance at 10 kHz.

3 Results

3.1 Compression Results

In this section we discuss the computational and experimental results of the four gyroid geometries in Table 1 under compression. **Figure 2A-B** and **Figure 2D-E** contain computer generated geometry (top left), the Von Mises stress from the FEA under $\varepsilon = 0.5$ compression (top right), the 3D printed 5x5x5 unit cell specimen prior to being tested (bottom left), and the 3D printed 5x5x5 unit cell specimen under $\varepsilon = 0.5$ compression (bottom right). The one exception is that the FEA data for SGp0.0 did not fully converge at $\varepsilon = 0.5$ and so the last converged data at $\varepsilon = 0.436$ was used for the FEA image in **Figure 2D**. Based on FEA models for each gyroid the stress does not localize, with the exception of SGp0.0, which has localized large stress points where self contact is occurring and likely causing the convergence issues. Based on visual comparisons of the images, the FEA models capture the deformation obtained experimentally. DGm0.7 is a notable exception where the sinusoidal curves on the front face of the FEA model uniformly deform into each other. The uniformity and spacing do not match in the 3D printed sample. The difference is from imperfections introduced during printing that causes misalignment of the sinusoidal curves as seen in the specimen prior to being tested. While loading the sample in compression, DGm0.7 undergoes some shearing during the compression load as a result of the offset sinusoidal curves.

One interesting deformation feature worth noting is the deformation of DGm0.2. The structure tends towards a layer by layer collapse. The experimental samples display a tendency for unit cell layers near the compression plates to collapse prior to the middle layers. Similar deformation patterns for this structure are reported in literature for gyroids made from PA 2200 (nylon 12 thermoplastic) [20, 21] and metal [18]. We believe the layers near the compression plates collapse first because they have the most distinct boundary conditions. Of course, this phenomenon does not occur in the FEA because there is only a single unit cell.

The plots in **Figure 2C,F** show the stress-strain curves for the data obtained from the FEA and experimental compression tests. We calculate stress as follows:

$$\sigma = F * A_{\text{composite}}^{-1} \quad (9)$$

where F is force and $A_{\text{composite}}$ is the cross sectional area of the composite. For example, the cross sectional area of one unit cell is 100 mm^2 ($10 \text{ mm} * 10 \text{ mm}$), and the cross sectional area of the 5x5x5 samples is $2,500 \text{ mm}^2$ ($50 \text{ mm} * 50 \text{ mm}$). The 3D printed specimens are compressed up to $\varepsilon = 0.5$ and unloaded. The data is an average of three samples, and the error bars represent one standard deviation. The stress-strain curves have residual strain and hysteresis for every geometry, which results from the viscoelastic material as seen in SI Appendix, Figure S2. The one exception to this is the hysteresis of DGm0.2 where the geometry appears to have increased the amount of hysteresis. FEA models have corresponding loading conditions up to $\varepsilon = 0.5$. The unloading curves for the FEA models are not plotted as they follow the same path as the loading curves. Thus, the FEA models do not capture the hysteresis and residual strain of the material.

The low volume fraction structures in **Figure 2C** show that SGp-1.2 is the most compliant structure of all the gyroids with a computationally predicted modulus of 7.7 kPa at $\varepsilon = 0.05$. SI Appendix, Figure S3 contains the curves for SGp-1.2 without DGm0.2 for better visualization. DGm0.2, despite having only a slightly higher volume fraction ($\phi = 0.13$ compared to $\phi = 0.1$), is significantly stiffer than SGp-1.2 with a computationally predicted modulus of 51.9 kPa at $\varepsilon = 0.05$. References[45, 46, 47] report similar trends where the sheet geometry, which we refer to as the matrix in this paper, has a higher stiffness than the network geometry (SGp, SGn, DGn). Note that the stress-strain curve for DGm0.2 starts out with an approximately linear response, and then becomes hypoelastic. The plateau in the curve corresponds to when the layers begin to collapse onto each other. The high volume fraction geometries in **Figure 2F** are stiffer than the low volume fraction geometries. DGm0.7 is the stiffest gyroid with a computationally predicted modulus of 293.4 kPa at $\phi = 0.05$, and SGp0.0 is closely behind with a modulus of 286.5 kPa at $\phi = 0.05$. Therefore, SGp-1.2 is over an order of magnitude more compliant than DGm0.7. It is interesting to point out the experimental curve for SGp0.0 because the curve contains two distinctively different slopes (

$\varepsilon = 0 - 0.35$ and $\varepsilon = 0.45 - 0.5$). The second slope of SGp0.0 approaches the slope of the solid SIL-30 from **Figure 1D** because after $\varepsilon = 0.45$ the gyroid has reached full collapse, and the structure behaves similarly to solid SIL-30. This also explains why the FEA solver struggles to converge after $\varepsilon = 0.436$ as a lot of contact occurs during full collapsing of the structure. Since the goal of the paper is to study the mechanical properties of the gyroid and not the mechanical properties of the fully collapsed gyroid, the FEA data for $\varepsilon = 0 - 0.436$ is sufficient for our analysis.

3.2 Tension Results

In this section, we discuss the computational and experimental results of the four gyroids in Table 1 under tensile loads. **Figure 3A-B** and **Figure 3D-E** contain computer generated geometry (top left), the von Mises stress from the FEA at $\varepsilon = 0.5$ (bottom left), the undeformed 3D printed 3x3x10 unit cell specimen (middle), and the 3D printed 3x3x10 unit cell specimen at $\varepsilon = 0.5$ (far right). Based on FEA models for each gyroid the stress does not localize and is fairly uniform throughout the structure, which indicates good stability for this geometry to support tensile loads. The FEA models capture the deformation obtained experimentally based on visual comparisons of the images.

The plots in **Figure 3C,F** show the stress-strain curves for the data obtained from the FEA and experimental tension tests. The 3D printed specimens are pulled in tension up to $\varepsilon = 0.5$ and unloaded. The data is an average of three identical samples, and the error bars represent one standard deviation. The stress-strain curves have minor residual strain and hysteresis for every geometry, which results from the viscoelastic material as seen in SI Appendix, Figure S2. FEA models have corresponding loading conditions up to $\varepsilon = 0.5$. The unloading curves for the FEA models are not plotted as they follow the same path as the loading curves. Thus, the FEA models do not capture the hysteresis and residual strain.

The low volume fraction geometries in **Figure 3C** show that SGp-1.2 is once again the most compliant of all the gyroids with a computationally predicted modulus of 10.7 kPa at $\varepsilon = 0.05$. SI Appendix, Figure S3 contains the curves for SGp-1.2 without DGm0.2 for better visualization. DGm0.2, despite having only a slightly higher volume fraction ($\phi = 0.13$ compared to $\phi = 0.1$) is significantly stiffer than SGp-1.2 with a computationally predicted modulus of 56.7 kPa at $\varepsilon = 0.5$. The high volume fraction structures in **Figure 3F** are stiffer than the low volume fraction structures. DGm0.7 is the stiffest gyroid with a computationally predicted modulus of 282.1 kPa at $\varepsilon = 0.05$, and SGp0.0 is closely behind with a modulus of 270.0 kPa at $\varepsilon = 0.05$. SI Appendix, Table S1 contains a complete list of modulus at $\varepsilon = 0.05$ for both the FEA and experimental data. The trend holds for compression and tension data where the most compliant geometry, SGp-1.2, is more than an order of magnitude more compliant than the stiffest geometry, DGm0.7. The large difference in stiffness makes the gyroid a good choice for mechanically tuning parts and an alternative to multimaterial printing.

3.3 Discussion

Comparing the compression data to the tension data, SI Appendix, Table S1 shows that the computationally predicted modulus is higher in compression for the high volume fraction geometries of SGp0.0 and DGm0.7 where as the computationally predicted modulus is higher in tension for the low volume fraction geometries of SGp-1.2 and DGm0.2. This data suggests that the higher volume fraction gyroids are stiffer in compression, and the lower volume fraction gyroids are stiffer in tension. The largest deviation between the computationally predicted modulus and the experimental modulus occurs with DGm0.2 geometry, which could be caused by a combination of misalignment of the porosity voids, worse printing resolution associated with the large surface area structure, parts

being printed thicker than the CAD model, and the affects of the thickness increasing radially.

To understand the discrepancies between the FEA and experimental data, SI Appendix, Figure S4 gives a side-by-side comparison of the CAD models and the printed samples before testing. From these images notice: (1) SGp-1.2 printed part is thicker than the CAD model, (2) SGp0.0 printed part is thicker and the circular void regions are slightly misaligned, (3) the aligned, crisp void circles of DGm0.2 CAD model and the oval, misaligned voids of the printed DGm0.2, (4) the large misalignment of the smaller voids for the DGm0.7 printed part. Additionally SI Appendix, Figure S5 provides CT scans for each of the gyroid compression samples. The visible discrepancy is that the thickness noticeably increases radially into the center of DGm0.2 and DGm0.7. The inconsistencies are from printer resolution and the inability to clean all the uncured resin off the parts before the thermal curing process. Another explanation for the discrepancies between the FEA data and the experimental data is due to the use of a representative volume element (single unit cell) and periodic boundary conditions which are used to model an infinitely large structure. The experimental models, on the other hand, are composed of 125 unit cells which is not well representative of an infinite system. However, the benefit of choosing a single unit cell and periodic boundary conditions for simulations is to be able to run faster simulations so that this work can be extended to analyze a larger design space of geometries.

Gibson and Ashby provide a relationship between elastic modulus and volume fraction[48]. The equation is

$$E_{latt.} = C_1 E_{sol.} \phi^n \quad (10)$$

where $E_{latt.}$ is the elastic modulus of the lattice, $E_{sol.}$ is the elastic modulus of the constituent material, C_1 is a prefactor, and n is a result of the deformation (stretch dominate ($n=1$) or bending dominate ($n=2$)). Fitting our single gyroid data to the power law equation in equation 10, we get $C_1 = 1.06$ and $n = 2.118$. Fitting our double gyroid matrix data to the power law equation, we get $C_1 = 0.703$ and $n = 1.32$. These values compare reasonably with other literature on gyroids, and the n values are reasonable for the dominant deformation mode expected for each gyroid type. [19] report a $C_1 = 1.02$ and $n = 2.4$ for single gyroid geometry fabricated from PA2200, and [20] report a $C_1 E_{sol} = 892$ and $n = 1.39$ for double gyroid matrix geometry made from PA2200.

3.4 Gyroid Capacitor

The compression and tension results show the gyroid's mechanical robustness as a composite. A second attractive quality of the gyroid is the large surface area to volume ratio. To demonstrate the novelty of using gyroid lattices for applications of multifunctional devices, we study a compliant gyroid capacitor. A compliant capacitor has the ability to bear load, store energy, and sense deformation by measuring changes in capacitance.

First, we leverage the geometry and mechanical analysis study above to design a soft capacitor. SGp, SGn, and DGm cannot produce a capacitor on their own because a capacitor needs two electrodes. We could design a capacitor using any combination of SGp, SGn, and DGm together. Given that SGp-1.2 produces the most compliant structure, we chose to design the capacitor using SGp-1.2 and SGn1.2 which together form the DGn1.2 (**Figure 4A**). While our previous mechanical experiments did not include DGn1.2, we hypothesize that the DGn1.2 force-strain curve would be approximately double that of the SGp-1.2 force-strain curve. We base the hypothesis on the fact that DGn1.2 contains the entire geometry of SGp-1.2 plus the SGn1.2 geometry. SGp-1.2 and SGn1.2 are similar in geometry, except that they have opposite chirality (given the corresponding t parameters).

Experimental data in SI Appendix, Figure S6 supports our hypothesis that the force-strain curve for DGn1.2 is approximately double the force of the SGp-1.2 curve.

Figure 4B shows the experimental setup of the capacitor undergoing a tension test. **Figure 4C** shows the relative capacitance, $\Delta C \cdot C_0^{-1}$ where ΔC is change in capacitance and C_0 is capacitance under no tension. We measure the capacitance at different strains for two experiments and the FEA model. EXP1 and EXP2 are the experimental tests of the same sample retested. Overall, the experimental tests produce good repeatability with minimal discrepancies between the FEA data and the experiment. One interesting aspect of the overall trend is that the capacitance first decreases with strain and then increases with strain. For $\varepsilon < 0.1$, the capacitance decreases with increasing strain. For $\varepsilon > 0.1$, the capacitance increases with increases in strain. The factors contributing to this trend include the changes in surface area and the distance between the electrodes as the device is pulled in tension. SI Appendix, Figure S7 shows how surface area is changing with strain and capacitance as the capacitor undergoes tension. The effect of the distance between electrodes changing is much more challenging to measure as a result of the complex geometry and nonuniformity produced by the boundary conditions during tensile loading. Some of the discrepancies between the FEA and the experiment could be from the FEA assuming high conductivity and low resistivity of the electrode material, which is a good assumption for metals but can produce discrepancies for carbon paint. Additionally, in the experiment the electrode resistance varies as the double gyroid capacitor is stretched and there is likely an uneven coating of carbon paint. At $\varepsilon = 0$, the FEA predicts 26.44 pF of capacitance, and the experiment predicts an average of 34.5 pF (as seen in SI Appendix, Figure S8). The mechanical response of the capacitor is in SI Appendix, Figure S9.

Here we demonstrate a capacitor over an order of magnitude more compliant than the constituent material and a surface area to volume ratio of 2.2 mm^{-1} (3893.2 mm^2 divided by 1750.3 mm^3). While we only study one combination of gyroid geometry for the multifunctional capacitor, other variation of SGp, SGn, DGM, and DGn could be studied. In summary, the DGn1.2 capacitor is an multifunctional embodied energy system whose structure is mechanically tuned for large compliance, geometry is a high surface area to volume ratio for producing a large capacitance, and structural deformation can be sensed from changes in capacitance.

4 Conclusion

Triply periodic minimal surface (TPMS) geometries like the gyroid offer mechanically robust composite structures with high surface area to volume ratios for coupling multiple functionalities. We studied four different gyroid geometries where we show over one order of magnitude difference in modulus is achievable between the most compliant and the stiffest gyroid studied. The FEA models show good visual deformation agreement with the deformed experimental samples. Given the lack of concentrated von Mises stress in the FEA models, the hyperelastic gyroids are robust structures under tension and compression loads. By using representative volume elements (RVE) and periodic boundary conditions (PBC) along with our scripted software, we have created a platform that can extend to other metamaterials and design optimization problems.

The double gyroid capacitor is a multifunctional device that embodies energy through the structural function of the gyroid (high compliance), storing electrical energy (large surface area to volume ratio of the gyroid structure), and sensing (estimating the deformation state by measuring the change in capacitance). The benefit of embodied energy systems is moving away from traditional robots and devices with isolated power, actuation, sensing, and control and towards multifunctional systems that can perform multiple functions simultaneously. Applications for our capacitor include soft robotics and wearables because a capacitor is a fundamental building block for storing energy and a deformable capacitor is important for self-sensing of deformation.

Supporting Information

Supporting Information is available from the Wiley Online Library or from the author.

Acknowledgements

This work was supported in part by the National Science Foundation (NSF), contract: 1825444 and IOS-2034351; NIH National Heart, Lung, and Blood Institute, contract: 5R01HL118019-07; Office of Naval Research, contract: N00014-22-1-2595; and Defense Advanced Research Project Agency Young Faculty Award, USA DARPA YFA, HR00112010004. This work made use of the Cornell Biotechnology Resource Center under the National Institutes of Health award No. S10OD025049.

References

- [1] K. Bertoldi, V. Vitelli, J. Christensen, M. v. Hecke, *Nature Reviews Materials* **2017**, 2, 17066 1.
- [2] M. Kadic, G. W. Milton, M. van Hecke, M. Wegener, *Nature Reviews Physics* **2019**, 1, 198.
- [3] S. C. L. Fischer, L. Hillen, C. Eberl, *Materials* **2020**, 13 1.
- [4] L.-y. Zhu, L. Li, Z.-a. Li, J.-p. Shi, W.-l. Tang, J.-q. Yang, Q. Jiang, *Journal of Translational Medicine* **2019**, 17, 89.
- [5] H. M. A. Kolken, S. Janbaz, S. M. A. Leeflang, K. Lietaert, H. H. Weinans, A. A. Zadpoor, *Materials Horizons* **2018**, 5 28.
- [6] J. M. Walker, E. Bodamer, A. Kleinfehn, Y. Luo, M. Becker, D. Dean, *Progress in Additive Manufacturing* **2017**, 2 99.
- [7] J. I. Lipton, R. MacCurdy, Z. Manchester, L. Chin, D. Cellucci, D. Rus, *Science* **2018**, 360, 6389 632.
- [8] D. Yang, B. Mosadegh, A. Ainla, B. Lee, F. Khashai, Z. Suo, K. Bertoldi, G. M. Whitesides, *Advanced Materials* **2015**, 27 6323.
- [9] M. Kaur, W. S. Kim, *Advanced Intelligent Systems* **2019**, 1 1900019.
- [10] C. Tawk, R. Mutlu, G. Alici, *Frontiers in Robotics and AI* **2022**, 8 1.
- [11] T. Chen, M. Pauly, P. M. Reis, *Nature* **2021**, 589 386.

- [12] H. Lee, Y. Jang, J. K. Choe, S. Lee, H. Song, J. P. Lee, N. Lone, J. Kim, *Science Robotics* **2020**, 5 1.
- [13] Y.-L. Wei, Q.-S. Yang, L.-H. Ma, R. Tao, J.-J. Shang, *Materials and Design* **2020**, 196 1.
- [14] J. Iyer, T. Moore, D. Nguyen, P. Roy, J. Stolaroff, *Applied Thermal Engineering* **2022**, 209 118192.
- [15] W. Li, G. Yu, Z. Yu, *Applied Thermal Engineering* **2020**, 179 115686.
- [16] J. G. Werner, G. G. Rodríguez-Calero, H. D. Abruña, U. Wiesner, *Energy and Environmental Science* **2018**, 11 1261.
- [17] D. Wei, M. R. J. Scherer, C. Bower, P. Andrew, T. Ryhänen, U. Steiner, *Nano Letters* **2012**, 12 1857.
- [18] I. Maskery, N. T. Aboulkhair, A. O. Aremu, C. J. Tuck, I. A. Ashcroft, *Additive Manufacturing* **2017**, 16 24.
- [19] I. Maskery, L. Sturm, A. O. Aremu, A. Panesar, C. B. Williams, C. J. Tuck, R. D. Wildman, I. A. Ashcroft, R. J. M. Hague, *Polymer* **2018**, 152 62.
- [20] D. W. Abueidda, M. Elhebeary, C.-s. A. Shiang, S. Pang, R. K. A. Al-rub, I. M. Jasiuk, *Material and Design* **2019**, 165, 107597 1.
- [21] D. W. Abueidda, M. Bakir, R. K. Abu Al-Rub, J. S. Bergström, N. A. Sobh, I. Jasiuk, *Materials and Design* **2017**, 122 255.
- [22] A. Ion, J. Frohnhofen, L. Wall, R. Kovacs, M. Alistar, J. Lindsay, P. Lopes, H.-T. Chen, P. Baudisch, In *Proceedings of the 29th Annual Symposium on User Interface Software and Technology*. ACM, Tokyo Japan, **2016** 529–539, URL <https://dl.acm.org/doi/10.1145/2984511.2984540> .
- [23] C. El-Helou, R. L. Harne, *Advanced Engineering Materials* **2019**, 21, 12 1900807.
- [24] S. Babaee, J. Shim, J. C. Weaver, E. R. Chen, N. Patel, K. Bertoldi, *Advanced Materials* **2013**, 25 5044.

- [25] M. R. O'Neill, D. Sessions, N. Arora, V. W. Chen, A. Juhl, G. H. Huff, S. Rudykh, R. F. Shepherd, P. R. Buskohl, *Advanced Materials Technologies* **2022**, 2200296 1.
- [26] S. Babaei, N. Viard, P. Wang, N. X. Fang, K. Bertoldi, *Advanced Materials* **2016**, 28 1631.
- [27] N. Fang, D. Xi, J. Xu, M. Ambati, W. Srituravanich, C. Sun, X. Zhang, *Nature Materials* **2006**, 5 452.
- [28] N. Sui, X. Yan, T.-Y. Huang, J. Xu, F.-G. Yuan, Y. Jing, *Applied Physics Letters* **2015**, 106 171905.
- [29] H.-W. Dong, S.-D. Zhao, Y.-S. Wang, L. Cheng, C. Zhang, *Journal of the Mechanics and Physics of Solids* **2020**, 137 103889.
- [30] Z. Liu, X. Zhang, Y. Mao, Y. Y. Zhu, Z. Yang, C. T. Chan, P. Sheng, *Science* **2000**, 289, 5485 1734.
- [31] X. An, C. Lai, H. Fan, C. Zhang, *International Journal of Solids and Structures* **2020**, 191–192 293.
- [32] C. Pouya, J. T. B. Overvelde, M. Kolle, J. Aizenberg, K. Bertoldi, J. C. Weaver, P. Vukusic, *Advanced Optical Materials* **2016**, 4 99.
- [33] M. Saba, M. Thiel, M. D. Turner, S. T. Hyde, M. Gu, K. Grosse-Brauckmann, D. N. Neshev, K. Mecke, G. E. Schröder-Turk, *Physical Review Letters* **2011**, 106 103902.
- [34] K. Hur, Y. Francescato, V. Giannini, S. A. Maier, R. G. Hennig, U. Wiesner, *Angewandte Chemie International Edition* **2011**, 50 11985.
- [35] Y. Jung, S. Torquato, *Physical Review E* **2005**, 72 1.
- [36] H. Montazerian, E. Davoodi, M. Asadi-Eydivand, J. Kadkhodapour, M. Solati-Hashjin, *Materials and Design* **2017**, 126 98.
- [37] Z. A. Qureshi, S. A. B. Al Omari, E. Elnajjar, F. Mahmoud, O. Al-Ketan, R. A. Al-Rub, *Case Studies in Thermal Engineering* **2021**, 27 101315.

- [38] O. Al-Ketan, R. K. A. Al-Rub, *Advanced Engineering Materials* **2019**, 21 1.
- [39] C. A. Aubin, B. Gorissen, E. Milana, P. R. Buskohl, N. Lazarus, G. A. Slipher, C. Keplinger, J. Bongard, F. Iida, J. A. Lewis, R. F. Shepherd, *Nature* **2022**, 602 393–402.
- [40] A. H. Schoen, In *NASA Technical Note TN D-5541*. **1970** 1–100.
- [41] M. R. J. Scherer, *Double-Gyroid-Structured Functional Materials: Synthesis and Applications*, Springer Theses. Springer International Publishing, **2013**.
- [42] H. G. von Schnering, R. Nesper, *Zeitschrift für Physik B Condensed Matter* **1991**, 83, 3 407–412.
- [43] D. Garoz, F. Gilabert, R. Sevenois, S. Spronk, W. Van Paepegem, *Composites Part B: Engineering* **2019**, 168 254.
- [44] W. Wu, J. Owino, A. Al-Ostaz, L. Cai, In *2014 SIMULIA Community Conference*. **2014** 707–719.
- [45] D. Li, W. Liao, N. Dai, Y. M. Xie, *Materials* **2019**, 12 2183.
- [46] S. C. Kapfer, S. T. Hyde, K. Mecke, C. H. Arns, G. E. Schröder-Turk, *Biomaterials* **2011**, 32 6875.
- [47] O. Al-Ketan, R. Rezgui, R. Rowshan, H. Du, N. X. Fang, R. K. Abu Al-Rub, *Advanced Engineering Materials* **2018**, 20 1800029.
- [48] L. Gibson, M. Ashby, *Cellular Solids: Structure and Properties*, Cambridge Solid State Science Series. Cambridge University Press, **1997**.

Table 1: Gyroid variations

Name	Gyroid	t	Volume Fraction, ϕ
SGp-1.2	SGp	-1.2	0.1
SGp0.0	SGp	0.0	0.5

DGm0.2	DGm	0.2	0.13
DGm0.7	DGm	0.7	0.46

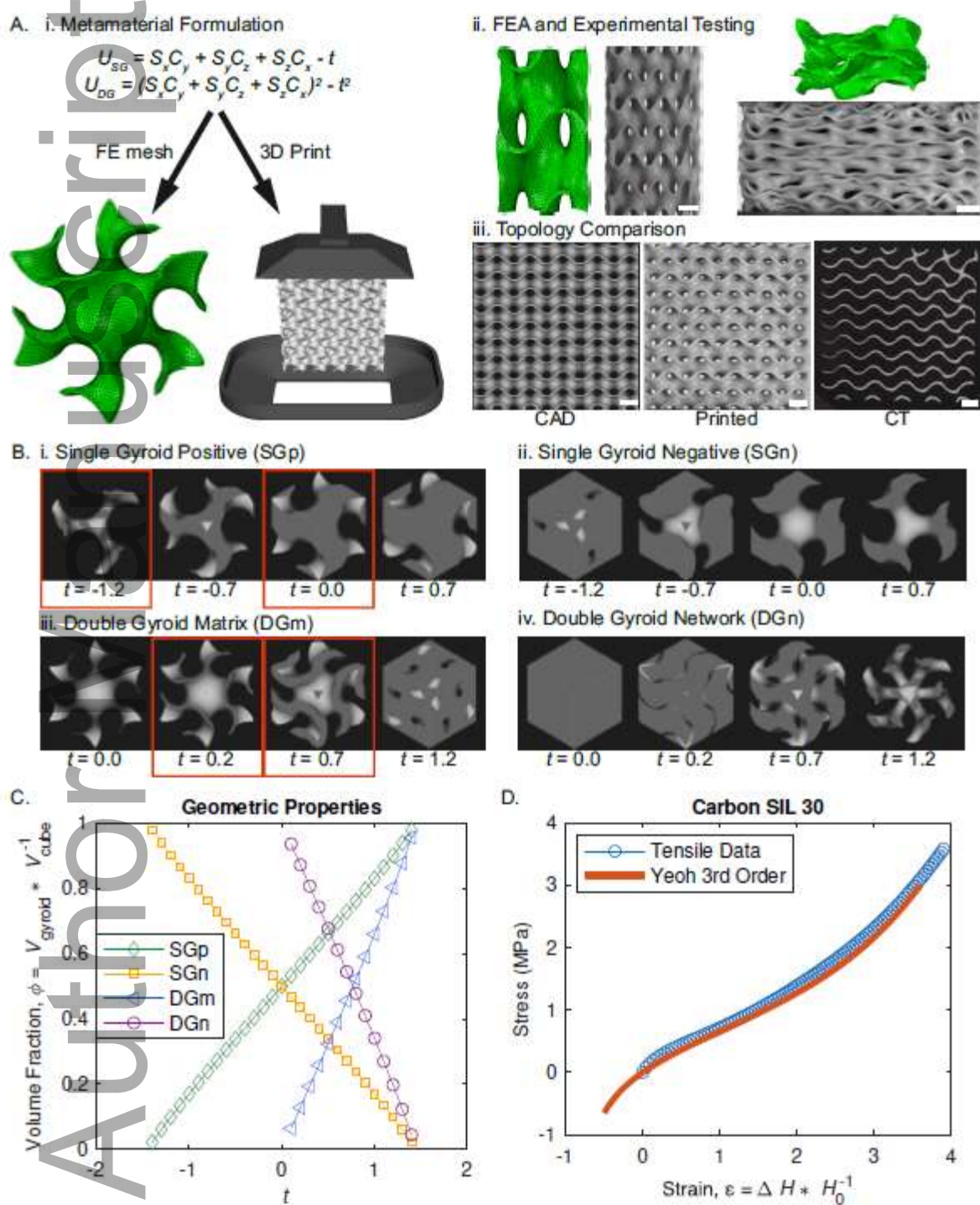


Figure 1: (A) Project overview: (Ai) Software is given the equations for the gyroid in nTopology to generate the finite element mesh (green image) and the files for 3D printing. (Aii) The software takes the finite element mesh files and runs a tension and compression analysis (green images). 3D printed samples undergo equivalent experimental test conditions to validate the FEA models. (Aiii) CT scans of the 3D printed specimen compared to the computer generated models. (B) Computer generated gyroids include: (Bi) single gyroid positive SGp, (Bii) single gyroid negative SGn, (Biii) double

gyroid matrix DGm, and (Biv) double gyroid network DGn. For each geometry, the corresponding t value from the equations in Ai are given. These images demonstrate how the gyroid changes with t . The four gyroids studied are outlined in red boxes. (C) Trends between the volume fraction and the gyroid equation parameter t . (D) Mechanical properties of SIL 30 and the Yeoh 3rd order material model. Tensile data provided by Carbon 3D Inc.

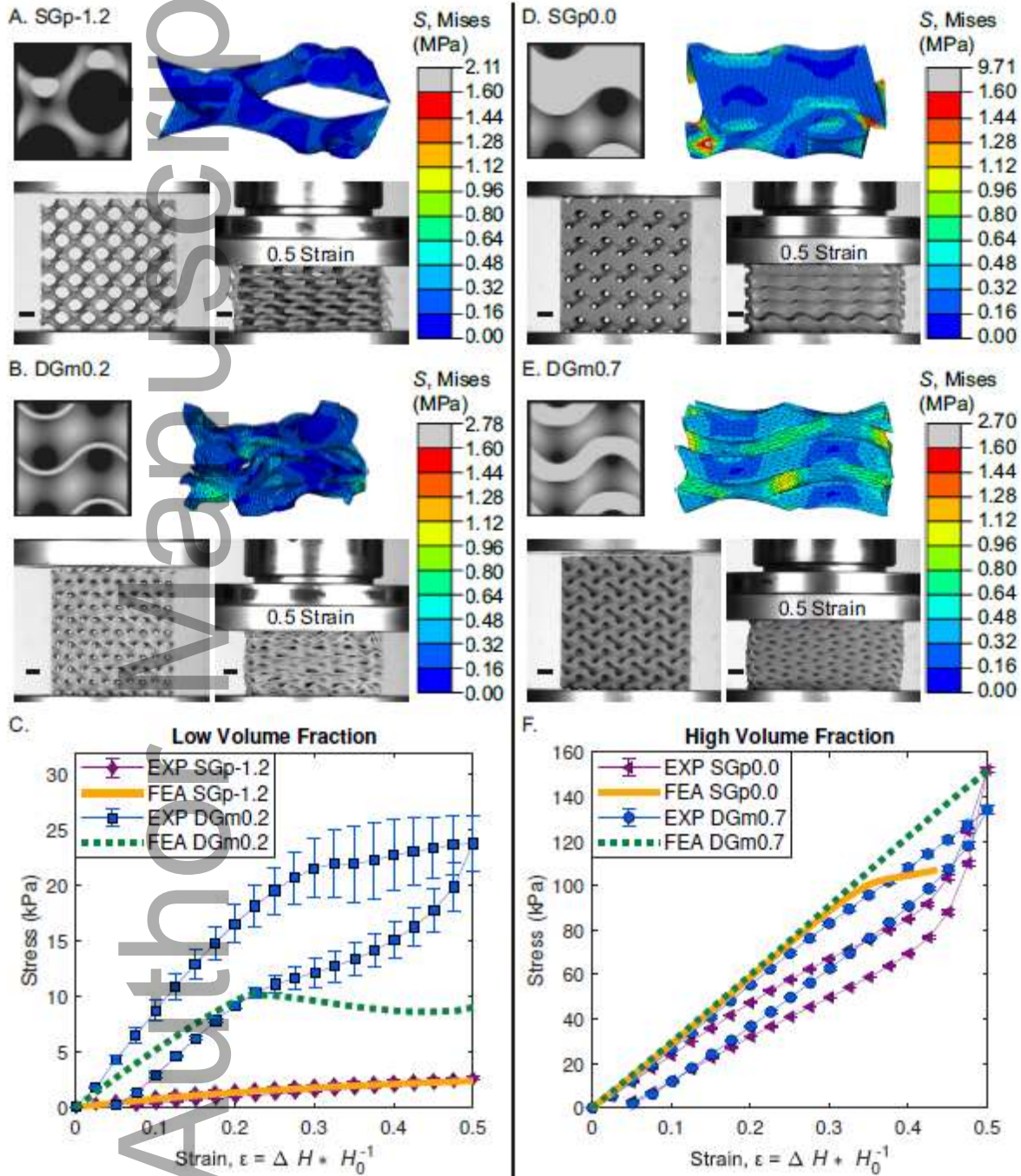


Figure 2: (A-C) Finite element analysis and experimental data of the low volume fraction geometries under compression. The geometries include the SGp-1.2 ($\phi = 0.1$) and DGm0.2 ($\phi = 0.13$). (D-F) Finite element analysis and experimental data of the high volume fraction geometries under compression. The geometries include the SGp0.0 ($\phi = 0.5$) and DGm0.7 ($\phi = 0.46$). (A,B,D,E) Top left: Computer generated geometry. Top right: Von Mises stress from the FEA under $\epsilon = 0.5$ (except SGp0.0 the last converged data/figure is at $\epsilon = 0.436$). Bottom left: 3D

printed 5x5x5 unit cell sample before being tested. Bottom right: 3D printed 5x5x5 unit cell sample under $\varepsilon = 0.5$. Scale bars are 5mm. (C,F) Error bars represent one standard deviation, and the markers represent the average of three samples.

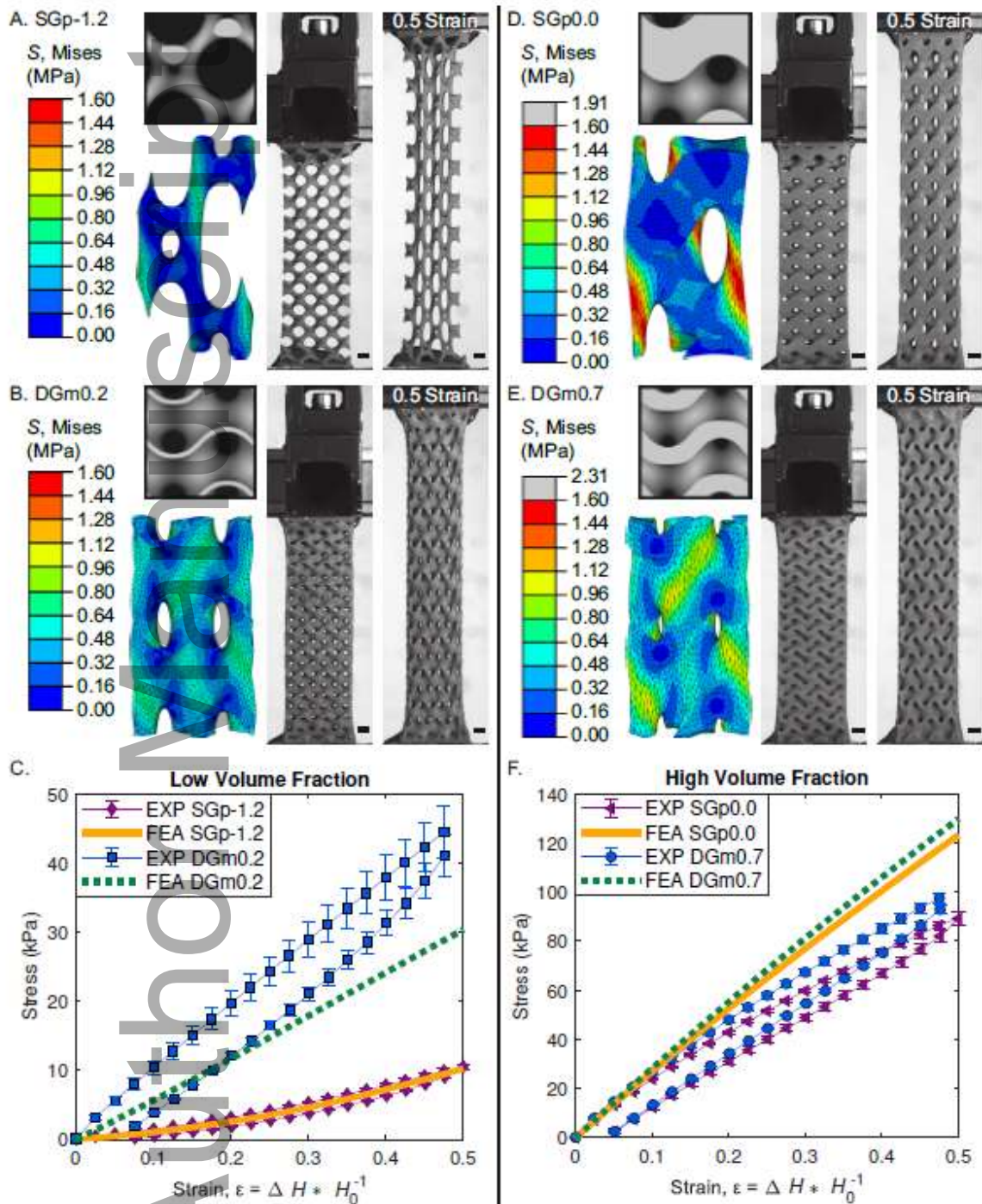


Figure 3: (A-C) Finite element analysis and experimental data of the low volume fraction geometries under tension. The geometries include the SGp-1.2 ($\phi = 0.1$) and DGm0.2 ($\phi = 0.13$). (D-F) Finite element analysis and experimental data of the high volume fraction geometries under tension. The geometries include the SGp0.0 ($\phi = 0.5$) and DGm0.7 ($\phi = 0.46$). (A,B,D,E) Top left: Computer generated geometry under no load. Bottom left: Von Mises stress from the FEA under $\varepsilon = 0.5$. Middle: 3D printed 3x3x10 unit cell sample before testing. Far right: 3D printed 3x3x10 unit cell sample under $\varepsilon = 0.5$. Scale bars are 5mm. (C,F) Error bars represent one standard deviation, and the markers represent the average of three samples.

This article is protected by copyright. All rights reserved

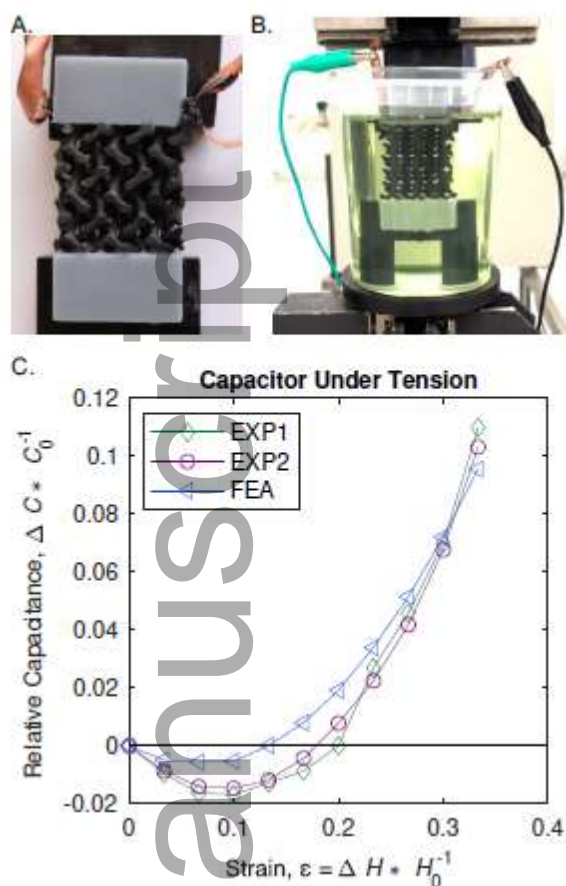


Figure 4: (A) Double gyroid capacitor with $t=1.2$ ($\phi=0.2$). We applied carbon paint to the networks. (B) Experimental setup for measuring the capacitance as the capacitor is pulled in tension. (C) Relative capacitance of DGn1.2 capacitor under different strains.

3D printed elastomeric gyroids tune nonlinear stress-strain curves not achievable with solid materials alone and change the compliance by two orders of magnitude. Gyroids have a large surface area to volume ratio which is beneficial for designing multifunctional devices. To demonstrate, authors fabricate a double gyroid capacitor that can simultaneously bear load, store energy, and sense.

